Numerical Analysis of Microstructure and Hardness Distribution in Fe-10Ni Welds

Experimentally validated numerical framework simulates thermal histories of multipass welding and maps the microstructure and hardness distribution in Fe-10Ni welds

BY S. MATAN AND B. ALEXANDROV

Abstract

Fe-10Ni is a high-strength, high-impact-toughness steel developed for naval structural applications. Gas metal arc welding in spray transfer mode (GMAW-s) with a Fe-10Ni filler metal produces welds with complex, deep, finger-like penetration profiles. The GMAW-s process is preferred for its higher productivity, but multipass groove welds exhibit lower impact toughness than those made with gas tungsten arc welding (GTAW). This study developed a numerical simulation framework to analyze microstructure and hardness distribution in multipass Fe-10Ni groove welds produced by GMAW-s. The framework utilized finite element analysis (FEA) models of GMAW-s processes for groove and bead-on-plate welds, a heat-source model reproducing the fusion-zone profile in GMAW-s welds, and experimentally derived thermal history–hardness and thermal history–microstructure relationships. The accuracy of the framework was confirmed by comparing FEA predictions with experimental results on heat-affected zone thermal histories and the spatial distributions of hardness and microstructure in multipass weld metal. Fe-10Ni weld metal exhibited a weak response to tempering by short-term subcritical reheats from multipass welding, resulting in a low weld metal hardness range, within 40 $HV_{0.2}$. However, the GMAW-s weld metal showed pronounced variation in the spatial distribution of as-solidified, reaustenitized, and tempered microstructures. As-solidified martensite, known to reduce impact toughness in Fe-10Ni welds, was found to occupy up to 0.43 fraction of the weld metal cross section. By linking thermal history to microstructure and properties, the proposed framework provides a pathway for computationally guided welding process optimization, aiming to reduce the regions of as-solidified martensitic microstructure and improve impact toughness in GMAW-s multipass Fe-10Ni welds.

Keywords

- Weld Modeling
- High Nickel Steel
- Process-Property Relationships
- Heat Source Modeling
- Phase Transformations

Introduction

The U.S. Navy has developed and commercialized a low-carbon, high-strength, and high-toughness steel based on the Fe-10wt-%Ni alloy system. This steel, which is more commonly known as Fe-10Ni, has been shown to have superior strength, ballistic, and toughness properties to the widely used HSLA-100 alloy (Ref. 1). The nominal chemical composition of the Fe-10Ni steel in wt-% is 0.1C, 9.64Ni, 1.53Mo, 0.06V, 0.65Cr, 0.64Mn, and 0.18Si (Ref. 2). The ultimate tensile strength (UTS) ranges between 125-150 ksi due to the presence of martensite across a wide range of cooling rates (Refs. 1–3), and the solid solution strengthening of Ni. Superior toughness (106 ft-lb at -84°C) and ballistic properties are provided by the low carbon content and nano-scale retained austenite between the martensite laths (Refs. 1, 2, 4). Upon sufficient stress and strain, the austenite transforms into

https://doi.org/10.29391/2026.105.015

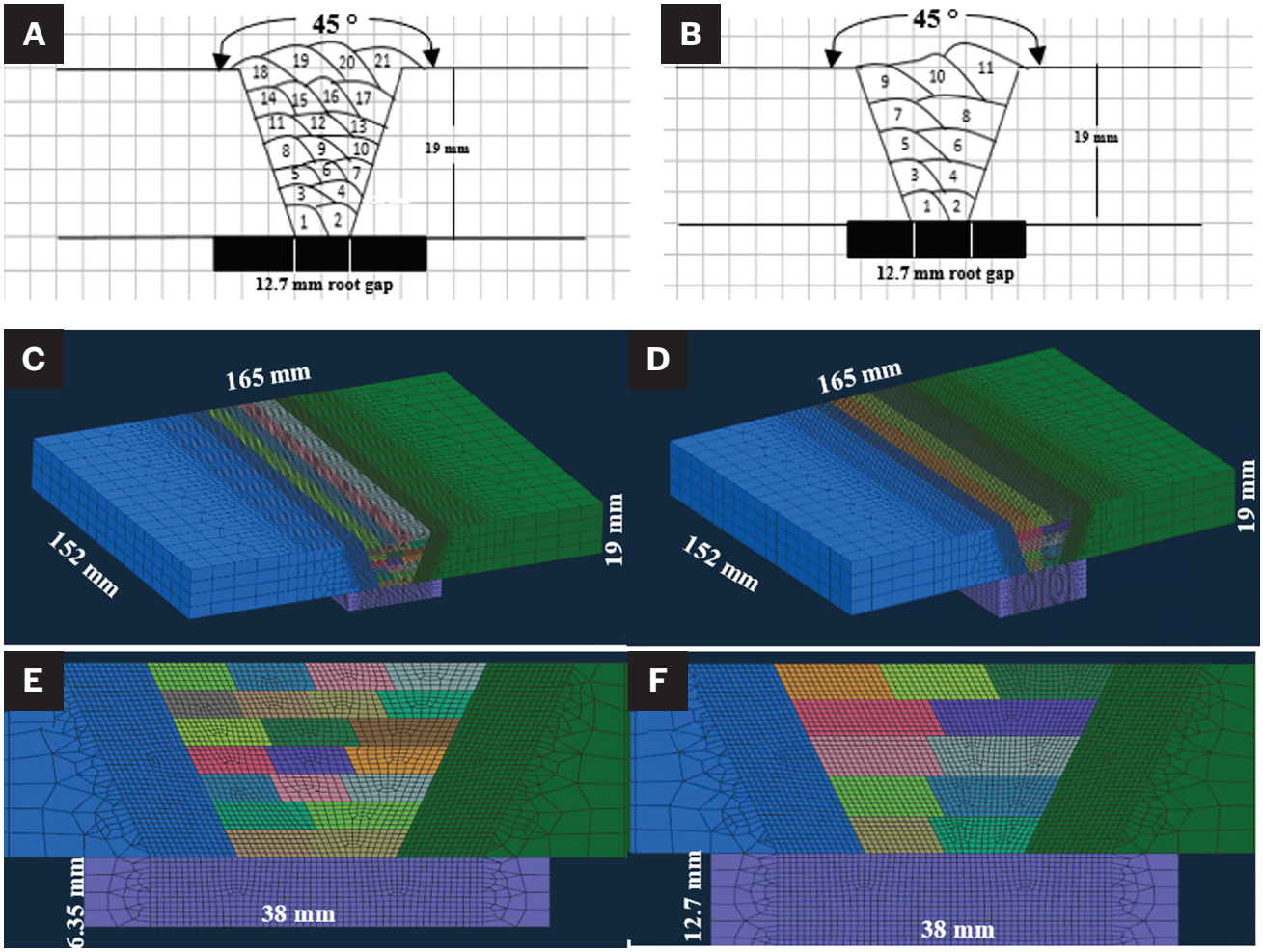


Fig. 1 — Joint geometry, full model dimensions, and halfway section of models: A, C, and E —LHI GMAW-s groove weld ; B, D and F — HHI GMAW-s groove weld.

martensite via a transformation-induced plasticity (TRIP) effect (Refs. 1, 4). The large amount of retained austenite (19%) in the Fe-10Ni steel is achieved by performing a complex three-step quenching–lamellarising–tempering (QLT) heat treatment (Refs. 1, 5–7).

Arc welding processes, such as gas metal arc welding (GMAW), are utilized in the construction of navy ships, and GMAW multipass groove welds are often made to join thicker sections. To produce matching welds, the U.S. Navy developed a high-strength, high-toughness solid wire welding electrode based on the Fe-10Ni alloy system (Refs. 8, 9). Fe-10Ni weld metal is fully martensitic with a significantly lower amount of retained austenite compared to the weld metal due to not undergoing QLT heat treatment (Refs. 9). The weld metal has demonstrated excellent mechanical properties for both the gas tungsten arc welding (GTAW) and GMAW processes (Refs. 10, 11). However, the impact toughness of the GTA weld metal is significantly higher than the GMA weld metal. The GMA welds were produced using the spray transfer process (GMAW-s) and a shielding composition of 98%Ar-2%O_2. This approach resulted in weld metal with higher oxide content and weld beads with a narrow and deep fingerlike characteristic (Ref. 10). The lower toughness of the GMAW-s welds was associated with non-uniform reaustenization and tempering caused by the irregular-shaped and fingerlike beads (Ref. 10). As-solidified, non-reaustenitized regions of the weld metal have been shown to promote cleavage fracture, which correlates with poor impact toughness (Ref. 10). However, the effect of multiple reheat thermal cycles, introduced by the multipass welding process, on the tempering response and microstructure of Fe-10Ni weld metals has yet to be investigated. Hardness reduction is often used to evaluate the material tempering response and can give insight into impact toughness behavior (Refs. 12–15).

Computational process modeling of GMAW-s can provide a pathway to quantify the influence of process parameters on hardness and microstructure in Fe-10Ni multipass welds. Previous studies (Refs. 16, 17) have highlighted the role of finite element analysis (FEA) in optimizing welding parameters by accurately predicting thermal cycles. Reliable modeling of the GMAW-s fusion zone profile requires precise calibration of heat sources to ensure that simulated weld geometries accurately reproduce experimental fusion profiles and thermal histories. Such accuracy is critical for enabling predictive process–property optimization.

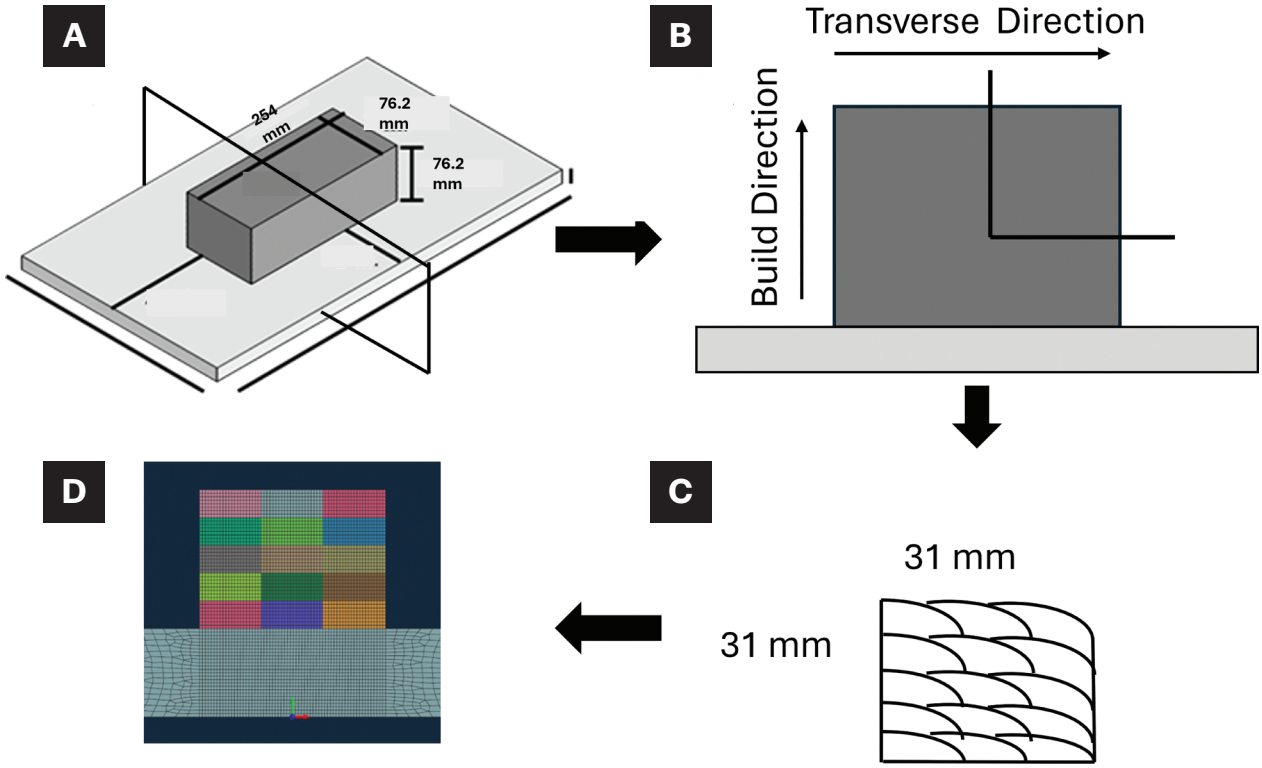


Fig. 2 — A — Dimensions of weld build-up; B — schematic detailing location of isolated region used for characterization; C — bead sequencing of isolated region; D — representative FEA model.

Table 1 — Composition of the Fe-10Ni Filler Metal and Undiluted Weld Metal Muildup, wt-%

	Fe	C	Ni	Mn	Mo	P	Si	V	Zr
Filler Metal	Bal.	0.017	9.61	0.78	0.66	0.009	0.45	0.16	0.003
Undiluted Buildup	Bal.	0.018	9.72	0.56	0.63	0.002	0.42	0.13	0

GMAW-s welds made with a 98%Ar-2%O_2 often produce a deep finger-like penetration profile (Refs. 18, 19). The thermal and kinetic energy generated by the high-frequency transfer of hot metal droplets results in deep-penetration fusion zones (Refs. 20–22). The O_2 in the shielding gas mixture alters the surface tension in the weld pool, thereby changing the molten fluid flow direction and causing a finger-like region in the weld profile (Refs. 10, 21). The widely used Goldak double-ellipsoidal heat-source model (Ref. 23) is effective for simulating regular-shaped fusion zones but cannot reproduce the fingerlike penetration observed in high-heat-input GMAW-s and pulsed GMAW (GMAW-p) processes.

Azar et al. utilized a coupled Goldak approach to try to replicate the deeper penetration profile produced by the GMAW-p process (Ref. 24). However, the welds produced in that study did not showcase the narrow and deep region seen in GMAW-s welds. Due to the similarities in shape between the GMAW-s weld bead profiles and laser and hybrid laser weld keyholes, studies modeling laser welding will be mentioned. Kik proposed a conical heat source stacked on a cylindrical heat source to represent the keyhole during laser welding (Ref. 25). Farrokhi et al. proposed a double cylindrical volumetric heat source to model deep penetration hybrid laser welding (Ref. 26). Chukkan et al. looked at three different heat source combinations: standalone conical, Goldak-Conical combination, and conical stacked cylindrical to model laser welding of 316L (Ref. 27). Although the heat sources mentioned can accurately model laser welding narrow penetration profiles, they cannot replicate the wider upper region of the penetration profiles produced by GMAW-s.

The objective of this study was to develop, validate, and demonstrate a numerical simulation framework for process-microstructure-properties analysis in GMAW-s multipass welds of Fe-10Ni steel. The goal was to quantify the spatial distribution of as-solidified, reaustenitized, and

tempered microstructures as a prerequisite for computational process-impact toughness optimization in such welds.

Materials and Methods

Experimental Welds and Weld Buildups

Two multipass groove welds were produced using GMAW-s process with low and high heat input (LHI and HHI, respectively) parameters and 98%Ar-2% O_2 shielding gas. The joint geometries are shown in Figs. 1A and B. Both welds were made on HY-130 base metal using Fe-10Ni solid wire filler metal. In addition, a weld buildup of undiluted Fe-10Ni weld metal was fabricated using a medium heat input (MHI) GMAW-s process. Specimens extracted from this buildup were used for thermal simulations to develop process-microstructure-property relationships. A region from the top-right quadrant, three beads wide and five layers high, was sectioned for metallurgical and microhardness characterization, as detailed in Fig. 2. The welding filler metal and undiluted weld buildup compositions, which were measured using optical emission spectrometry, and the GMAW-s welding parameters are provided in Tables 1 and 2, respectively.

A weld overlay of Fe-10Ni filler metal was deposited on a low-carbon steel plate using GMAW-s LHI process. The top surface of the butter layers was machined flat. Three sets of holes were drilled from the backside of the plate into the

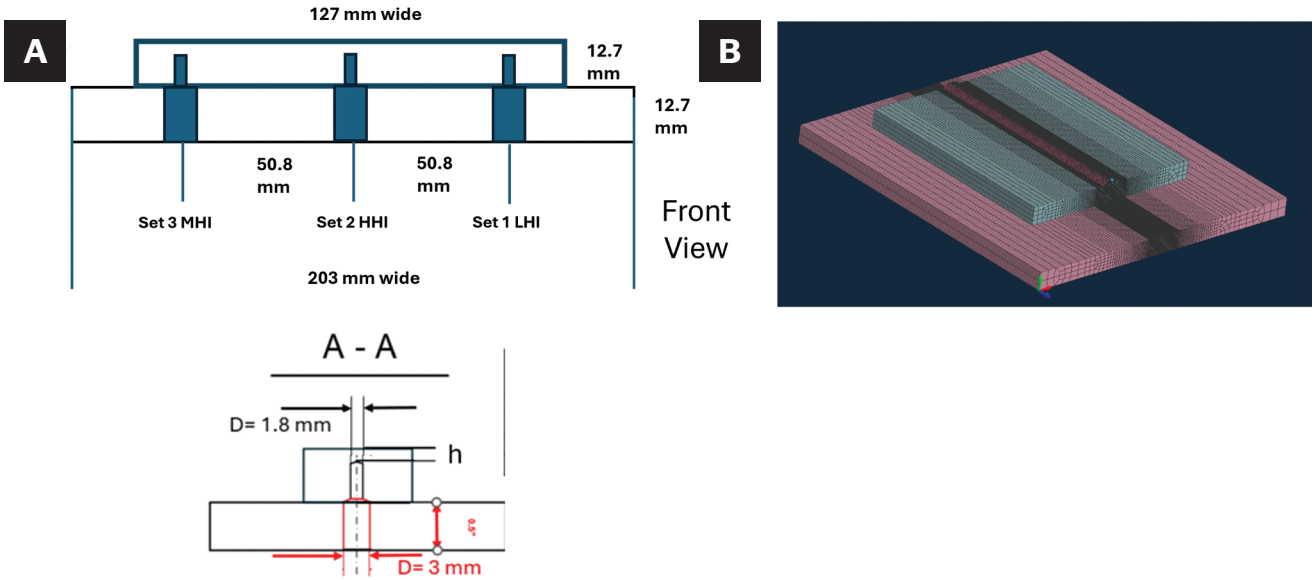


Fig. 3 — A — Schematic of Fe-10Ni overlay on low alloy steel plate showing thermocouple (TC) hole locations and TC hole dimensions; B — corresponding BoP FEA model.

Table 2 — GMAW-s Process Parameters

	LHI	HHI	MHI
Current (A)	300	300	300
Voltage (V)	26.1	26.1	26.1
Wire Feed Speed (mm/s)	150	150	150
Travel Speed (mm/s)	7.9	3.7	5.04
Heat Input (J/mm)	993.1	2204	1574
Preheat (C)	121	121	121
Interpass (C)	121-150	121-151	121-151
Passes	21	11	162

butter layers, as detailed in Fig. 3. The distances *h* from the hole tips to the overlay top surface corresponded to heat-affected zone (HAZ) locations in bead-on-plate (BoP) welds made with GMAW-s LHI, MHI, and HHI processes. Type K thermocouples (TCs) were capacitor-discharge welded into the hole tips. BoP welds were made directly above each TC set using the respective GMAW-s parameters listed in Table 2. Thermal cycles were recorded at 10kHz frequency using an instruNet i100 data acquisition system. The recorded thermal histories were used to calibrate and validate the numerical

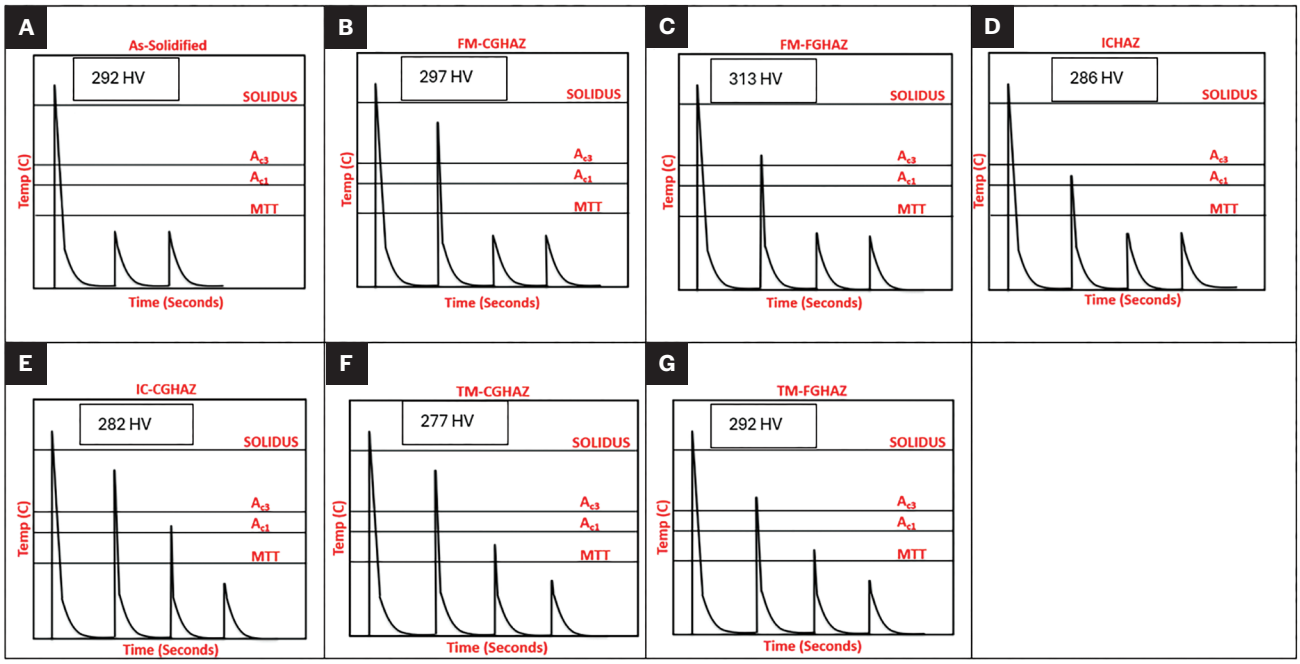


Fig. 4 — Example thermal histories of weld metal microstructural categories: A — As-solidified weld metal; B — fresh martensite – CGHAZ; C — fresh martensite – FGHAZ; D — ICHAZ; E — intercritically reheated – CGHAZ; F — tempered martensite – CGHAZ; G — tempered martensite – FGHAZ.

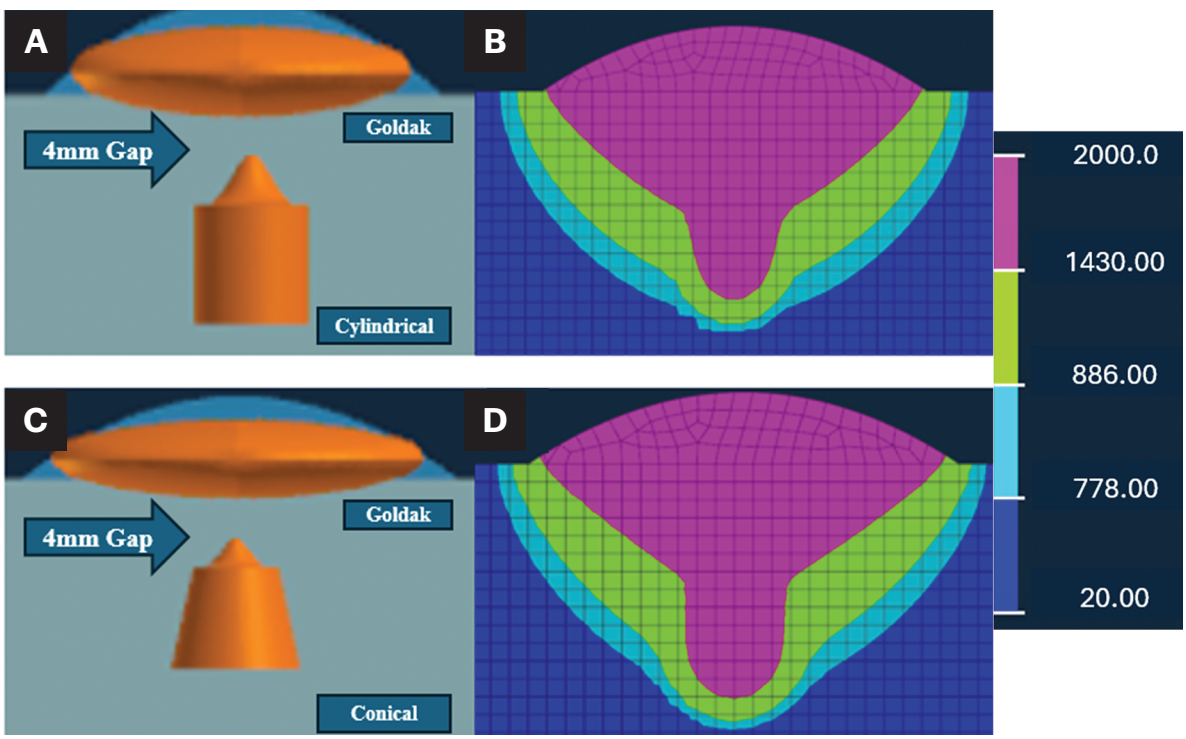


Fig. 5 — 3D visualization and FEA simulated weld profiles generated using Goldak/Cylindrical HS vs. Goldak/Conical HS with a wider bottom radius: A and B — Goldak/Cylindrical HS; C and D — Goldak/Conical HS.

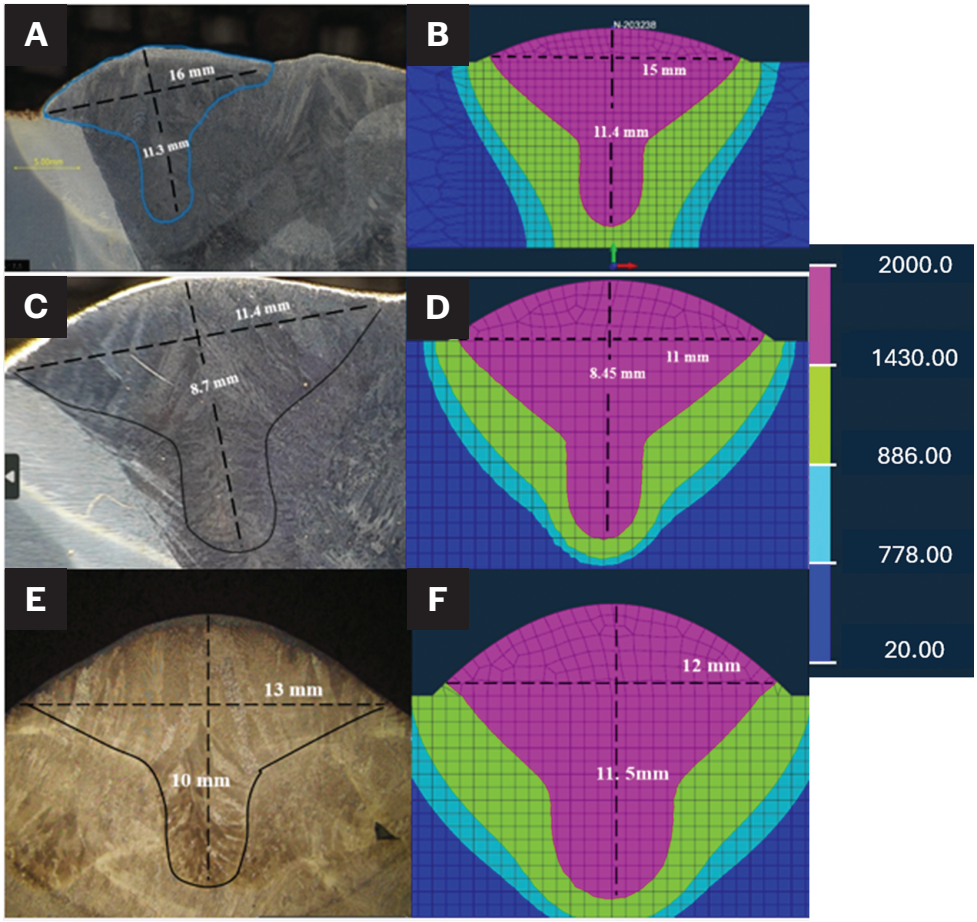


Fig. 6 — Comparison between experimental (A, C, E) and simulated (B, D, F) single-bead weld profile: A and B — HHI; C and D — LHI; E and F — MHI.

heat sources described later on. The weld overlay prevented dilution from the low-carbon substrate and ensured that the recorded thermal cycles reflected the thermophysical properties of undiluted Fe-10Ni weld metal.

Development of Thermal History - Microstructure - Hardness Relationships

To quantify the effect of multiple reheat thermal histories during multipass welding on the microstructure and hardness/tempering of the martensite in Fe-10Ni weld metal, thermal history-microstructure-hardness relationships were developed. Round specimens (6.35 mm diameter × 63 mm length) were machined along the welding direction of the Fe-10Ni buildup and subjected to thermal simulations using a Gleeble™ 3800 thermo-mechanical simulator. Critical transformation temperatures (A_{C1}, A_{C3}, M_S, and M_F) were determined by heating specimens to 1350°C at 100°C/s, followed by free cooling via a 10 mm free span, resulting in an average cooling rate of ~70°C/s in the temperature range between 1350°C and 500°C. The free span in the Gleeble system is the distance between the copper jaws, which influences heat extraction during cooling. Dilatometry was performed following ASTM A1033-18 (Ref. 27). Thermal cycles representative of key HAZ subregions were simulated using the same heating and cooling rates. Peak temperatures were set at 1350°C for coarse-grained HAZ (CGHAZ), 1000°C for fine-grained HAZ (FGHAZ), 700°C for intercritical HAZ (ICHAZ), and a double cycle of 1350°C followed by 700°C for intercritically reheated CGHAZ (IC-CGHAZ). This enabled controlled replication of microstructural evolution associated with multipass welding.

To determine the minimum tempering temperature (MTT), CGHAZ-simulated specimens were reheated to sub-A_{C1} peak temperatures of 500, 550, 600, and 650°C. The MTT is defined as the lowest subcritical temperature that causes measurable hardness reduction due to tempering (Refs. 16, 17). This distinction is critical for differentiating between fresh and tempered martensite and informs the thermal history and microstructure relationships. In addition to single reheats, several specimens were subjected to four sequential reheats to the determined MTT to replicate repeated subcritical thermal cycling typical of multipass welding. This enabled assessment of cumulative thermal effects on hardness and microstructure.

All thermally simulated specimens, including HAZ, single reheat, and multi-reheat conditions, were cross-sectioned and tested for macro-hardness using a LECO indenter with a 10 kg load. Hardness data from the experimental weld buildup cap pass served as the as-solidified hardness. These results

Table 3 — Description of Microstructural Categories for Thermal History-Microstructure Relationship Development

As Solidified - Figure 4A (292 HV)	Solidified weld metal that didn't receive a thermal cycle above MTT, A_{C1} or A_{C3}
FM-CGHAZ - Figure 4B (297 HV)	Weld metal that has been reheated above 1200°C, forming fresh martensite, which has not received a tempering cycle
FM-FGHAZ - Figure 4C (313 HV)	Weld metal that has been reheated above A_{C3} but below 1200°C, forming fresh martensite, which has not received a tempering cycle
ICHAZ - Figure 4D (286 HV)	Weld metal that has been reheated between A_{C1} and A_{C3} and didn't receive a tempering cycle
IC-CGHAZ - Figure 4E (282 HV)	Weld metal that was reheated above 1200°C, then reheated once again between A_{C1} and A_{C3}
TM-CGHAZ - Figure 4F (277 HV)	Weld metal that has been reheated above 1200°C and received a tempering cycle above MTT
TM-FGHAZ - Figure 4G (292 HV)	Weld metal that has been reheated above A_{C3} but below 1150°C and received a tempering cycle

FM - fresh martensite, TM - tempered martensite

were used to develop correlations between thermal history and weld metal hardness.

Depending on the thermal histories experienced, Fe-10Ni weld metal can exhibit a range of microstructures, including fresh (FM) and tempered martensite (TM) as well as the as-solidified microstructure and/or various weld metal HAZ subregions. To systematically describe these variations, several microstructural categories were established to represent the full spectrum of microstructures observed in Fe-10Ni multipass groove welds. These categories and their corresponding thermal histories are detailed in Table 3 and illustrated in Fig. 4.

In defining these categories, a cutoff of 1200°C was selected to distinguish where the FGHAZ ends and the CGHAZ begins. The representative Gleeble thermal cycles described earlier (1000°C for FGHAZ and 1350°C for CGHAZ) were chosen as single-temperature cycles, but the full microstructural range spans a broader temperature window. Specifically, any peak temperature above 1200°C is classified as CGHAZ, while peak temperatures between A_{C3} and 1200°C fall within the FGHAZ range in Table 3 and Fig. 4. Finally, each category is further separated into FM or TM, depending on whether the region experienced a reheating cycle above the MTT, which will be quantified in the results.

Metallurgical Characterization

Cross sections of the LHI, MHI, and HHI welds were prepared using standard metallographic techniques and etched with 2% Nital to reveal bead profiles. For the MHI weld buildup, a final polish with 0.05 µm colloidal silica for 10 minutes was performed to enable characterization using electron backscatter diffraction (EBSD). A selected region of the Fe-10Ni buildup, measuring 25 mm wide × 15 mm long, was scanned using a ThermoFisher Quattro ESEM. Multiple EBSD maps were acquired at 65× magnification with a 3 µm step size and stitched using EDAX OIM Analysis™ v9 software. Grain size was calculated using the equivalent circle diameter (ECD) method in OIM Analysis™ v9, with grains reconstructed at a 15 deg. grain tolerance angle and a minimum grain size of 5 pixels, per ASTM E2627 (Refs. 29, 30). Microhardness mapping was performed across the Fe-10Ni buildup using a Leco LM-100AT indenter with a 200 g load and 0.35 mm spacing.

Computational Modeling

FEA Model Development and Simulation Setup

FEA models of the LHI and HHI multipass groove welds, MHI weld buildup, and BoP welds were developed using SysWeld™ software. The LHI and HHI models, shown in Figs. 1C and E and Figs. 1D and F, respectively, were constructed to match the cross-sections of the experimental groove welds depicted in Figs. 1A and B. The MHI model was designed to replicate the upper-right quadrant of the weld buildup illustrated in Fig. 2. The BoP model is identical to the experimentally welded BoP configuration shown in Fig. 3B.

In the groove welds, the weld beads in each layer were modeled using parallelograms and trapezoids, as shown in

Table 4 — Heat Source Parameters for the GMAW-s LHI, HHI, and MHI Processes

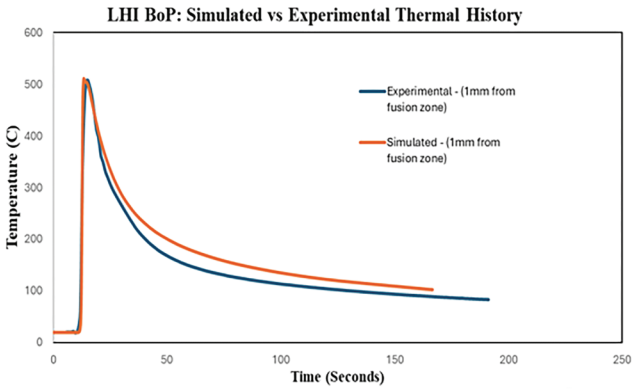
	LHI Weld		HHI Weld		MHI Weld	
	Goldak HS	Cylindrical HS	Goldak HS	Cylindrical HS	Goldak HS	Cylindrical HS
Travel Speed (mm/s)	7.9	7.9	3.7	3.7	5.04	5.04
Heat Input (J/mm)	725	268	1600	604	1000	574
Goldak HS Length and Cylindrical HS Upper Radius	6	2	8	3	8	2
Goldak HS Width and Cylindrical HS Lower Radius	10	3	16	4	13	3
Goldak HS Penetration and Cylindrical HS Height	1	3	0.5	5	1	3
Arc Efficiency	0.8	0.8	0.8	0.8	0.8	0.8
Goldak Length Ratio (Front/ Back Ellipsoid)	1	N/A	1	N/A	1	N/A
Goldak Power Ratio (Front/ Back Ellipsoid)	1	"	1	"	1	"
Advanced Controls (Gap between Heat Source Positions)	Z:0 X:0 Y:0	Z: -4 X:0 Y:0	Z:0 X:0 Y:0	Z: -4 X:0 Y:0	Z:0 X:0 Y:0	Z: -4 X:0 Y:0

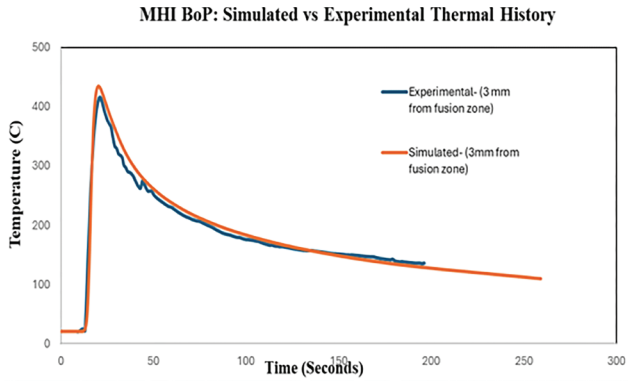
Table 5 — Comparison of Simulated and Predicted Thermal Histories

Heat Input	Simulated Peak Temperature (°C)	Experimental Peak Temperature (°C)	Simulated $t_{8/5}$ (°C/s)	Experimental $t_{8/5}$ (°C/s)
LHI	511	507	–	–
MHI	433	416	–	–
HHI	998	980	25	24.8

Figs. 1E and F. This approach allowed the modelling of the observed bead overlaps, while enabling automated mesh generation in the respective FEA models. The weld buildup model used a rectangular bead profile (Fig. 2D). A fine mesh size of 0.5 mm was applied in the fusion zone and HAZ, the primary areas of interest, while mesh density was gradually coarsened in the surrounding regions.

Thermal simulations for all four models were performed in SysWeld™. The LHI and HHI groove weld simulations utilized Fe-10Ni and HY-130 databases for the weld metal and base metal thermophysical properties, respectively. The MHI buildup and BoP models utilized the Fe-10Ni database. The Fe-10Ni database was manually developed and generated in SysWeld™ using experimentally obtained thermophysical temperature-dependent data. The HY-130 thermophysical properties database was generated using Thermo-Calc Software TCFE14 Steels/Fe-alloys Database (Ref. 31). The initial temperature was set to 20°C, and cooling due to convection was applied to all free surfaces with a heat transfer coefficient of 25 W/m²·C. The FEA models were clamped on all four corners, with the clamp locations being constrained in all directions. The SysWeld™ simulations were performed using the welding parameters and calibrated heat sources defined in Tables 2 and 4, respectively. The simulations predicted the local thermal cycles in the multipass groove





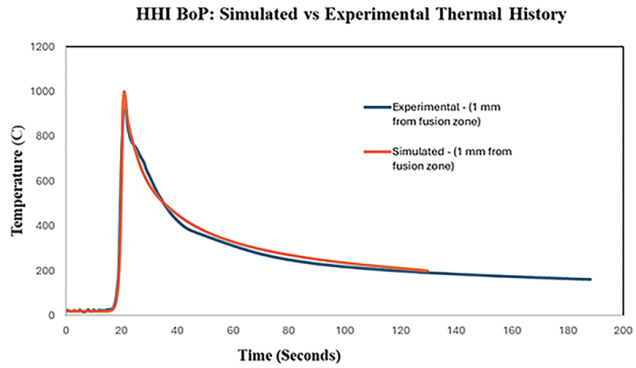


Fig. 7 — Comparison of FEA predicted thermal cycles to in-situ measured thermal histories for LHI, MHI, and HHI BoP welds.

welds and the weld buildup. These predicted thermal cycles were used with the thermal history–property relationships detailed in results to determine the local hardnesses and microstructure and generate hardness and microstructure contour maps in LHI, MHI, and HHI Fe-10Ni welds.

Heat Sources Development and Calibration

Due to the unique bead profiles produced by the GMAW-s process, a combination of heat sources was used to accurately represent the experimental weld profiles. To replicate the finger-like penetration profile of the GMAW-s process, we developed an approach that uses a Goldak heat source (HS) model (Ref. 23) on top of a Gaussian cylindrical HS. A similar stacking approach was explored by Champagne and Pham (Ref. 32), who combined a Gaussian disc heat source with a Gaussian cylindrical heat source. However, our method diverges from the cylindrical shape, as will be detailed shortly. In this study, Goldak's moving HS (Ref. 23) was used to model the upper portion of the GMAW-s fusion zone. It utilizes two ellipsoids, Eq. 1 and Eq. 2, one in the front and one in the rear of the fusion zone, to model the energy distribution of arc welding processes:

$$Q_f(x,y,z) = \frac{6\sqrt{3} f_f Q}{abc_f \pi\sqrt{\pi}} exp\left(-3\frac{x^2}{a^2} - 3\frac{y^2}{b^2} - 3\frac{z^2}{c^2}\right) \quad (1)$$

$$Q_r(x,y,z) = \frac{6\sqrt{3} f_r Q}{abc_r \pi\sqrt{\pi}} exp\left(-3\frac{x^2}{a^2} - 3\frac{y^2}{b^2} - 3\frac{z^2}{c^2}\right) \quad (2)$$

where Q_f and Q_r are heat flux densities of the front and rear ellipsoids, f_f and f_r, are the fractions of power distribution between the ellipsoids, and a, b, and c are the semi-axis of the ellipsoids (Ref. 23).

The Gaussian cylindrical HS, Equation 3 and Equation 4, was utilized to model the fingerlike region of GMAW-s weld (Refs. 25, 33):

$$Q(x,y,z) = Qexp\left(-\frac{x^2+y^2}{r_0^2(z)}\right) \quad (3)$$

$$r_0 = r_e + \frac{r_i - r_e}{z_i - z_e}(z - z_e) \quad (4)$$

where Q is the volumetric heat flux density for the heat source, r_e and r_i are the upper and bottom radii, and z_e and z_i define the HS height.

The combined Goldak/Cylindrical Gaussian approach was used to calibrate heat sources for FEA simulations of the LHI, MHI, and HHI GMAW processes. A custom material database for Fe-10Ni steel, based on experimentally measured temperature-dependent thermal conductivity, heat capacity, and density, was used to define the weld metal's thermo-physical properties. Fe-10Ni properties were predicted for both the weld and base material in the BoP models.

Fusion zone profiles were simulated using a combined HS consisting of a Goldak double ellipsoidal model positioned at the top of the weld bead and a cylindrical Gaussian HS placed 4 mm below, as seen in Fig. 5. This configuration allowed the two heat source regions to merge and produce the desired fusion zone shape. When the top and bottom diameters of the cylindrical source were equal, simulations resulted in a deep, narrow finger with a wider top (Figs. 5A and B). This wider top occurred because the upper part of the finger was influenced by both heat sources. Increasing the bottom radius to create a truncated conical shape improved heat distribution at the base and straightened the finger-like profile, resulting in better agreement with experimental welds, Figs. 5C and

Table 6 — Effect of Subcritical Temperature Reheats on CGHAZ Hardness: Quantification of MTT

Thermal Cycle	HV_{10}*	Standard Deviation
CGHAZ	297	3.14
500 Reheat	293	2.72
550 Reheat	298	1.56
600 Reheat	292	2.42
650 Reheat	277	2.17
650 × 4 reheat	271	2.94

* Average of 5 measurements

D. This improved configuration is referred to as the Goldak/Conical HS. Figure 5 compares the simulated fusion zones using the Goldak/Cylindrical HS and the Goldak/Conical HS, showing that the latter produced a more accurate match to the experimental Fe-10Ni weld profile shown in Figs. 6A, 6C, and 6E.

During calibration, arc efficiency and heat source parameters were manually adjusted to reproduce the experimentally observed fusion zones. An initial arc efficiency of 0.84, based on values reported by DuPont and Marder (Ref. 34) for GMAW, but a final value of 0.80 provided the best agreement with measured thermal histories (Fig. 7). The heat input was distributed with 76% allocated to the Goldak source and 24% to the conical source, which most accurately captured the fusion zone geometry.

For validation, Fig. 6 compares the FEA-predicted fusion zone profiles generated using the calibrated LHI, MHI, and HHI heat sources with the corresponding experimental profiles. For the LHI and HHI conditions, the cap passes from the experimental groove welds were used for comparison, as they represent the final fusion zone without remelting from additional passes. For the MHI condition, the fusion zone profile from the experimental MHI BoP weld cross-section was used. Depth and width measurements of the fusion zones from all three cases are shown in Fig. 5. The final heat source parameters for LHI, MHI, and HHI are provided in Table 4.

The calibrated heat sources were further validated by comparing simulated thermal histories to the experimental data. As shown in Fig. 7, the predicted thermal cycles closely matched the recorded histories. Table 5 compares experimental and simulated peak temperatures for the LHI, MHI, and HHI BoP welds, along with the $t_{8/5}$ cooling time for the HHI condition. Accurate prediction of both high and low peak temperatures is critical for reliable modeling of microstructural evolution and hardness distribution. High peak temperatures determine whether the material reaches the austenite region, which influences the formation of microstructural zones such as the FGHAZ and CGHAZ and directly affects local hardness. Low peak temperatures are equally important, as they govern the extent of intercritical reheating and the degree of tempering in previously heated regions. The close agreement between the fusion zone profiles (Fig. 6) and the thermal histories (Fig. 7 and Table 5) confirms that the combined heat-source approach effectively models Fe-10Ni welds produced with the GMAW-s process and the selected shielding gas composition.

Results and Discussion

Development of Thermal History-Microstructure-Hardness Relationship for Fe-10Ni Weld Metal

Thermal history-microstructure-hardness relationships were developed to evaluate the effects of multiple subcritical and supercritical reheats, commonly encountered in multipass welding, on the hardness behavior of Fe-10Ni weld metal. The critical transformation temperatures were first determined using dilatometry with five replicate tests. Figure 8A shows a dilatometry curve obtained from Gleeble testing at a cooling rate of 70°C/s. Transformation temperatures are indicated by tangent lines drawn on the curves. The Fe-10Ni weld metal exhibited A_{C1} and A_{C3} temperatures of 686°C ± 7 and 725°C ± 10, respectively. Previous studies have reported that Fe-10Ni transforms to martensite over a wide range of welding cooling rates (Refs. 3, 9, 35). Based on this, the lower-temperature transformations are identified as the martensite start (MS) and martensite finish (MF) temperatures, which are 399°C ± 5 and 217°C ± 8, respectively.

Figure 9A and Table 6 summarize the hardness values of CGHAZ Gleeble-simulated samples subjected to subcritical temperature reheats. The baseline CGHAZ sample had a hardness of 298 HV_{10}. Subsequent reheats produced little to no hardness drop until a peak reheat temperature of 650°C was reached. A consistent 20 HV_{10} hardness drop was observed at reheating to 650°C, which is near the A_{C1} temperature of 686°C for Fe-10Ni. Dilatometry testing was performed on the 650°C reheat sample (Fig. 8B), and no sign of dilation due to a phase transformation was observed. Therefore, the hardness

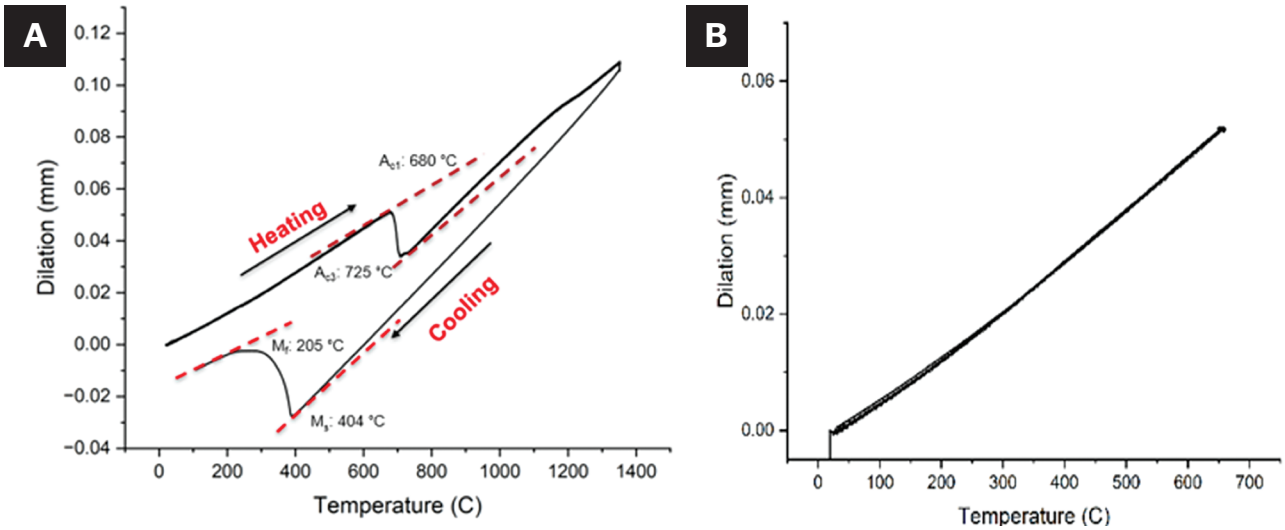


Fig. 8 — Dilation curve for Fe-10Ni GMA weld metal with 100°C/s heating rate and 70°C/s cooling rate: A — 1350°C peak temperature; B — 650°C peak temperature

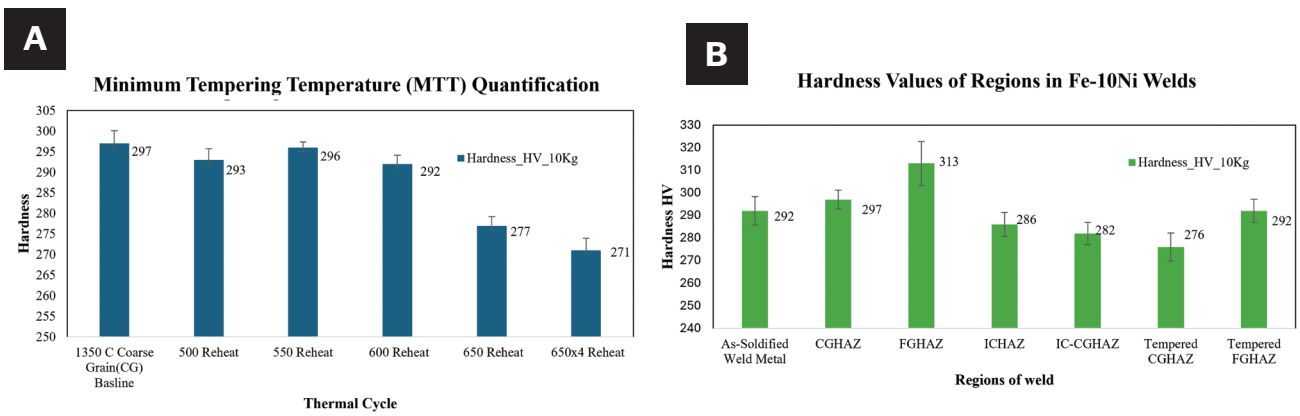


Fig. 9 — Fe-10Ni weld metal hardness measurements: A — CGHAZ hardness for various peak temperature reheats; B — hardness of the various regions observed in Fe-10Ni multipass welds.

drop was attributed to tempering of the fresh martensite in the initial CGHAZ microstructure, and 625°C was defined as the MTT of the Fe-10Ni weld metal because it lies between 600°C, where tempering does not occur, and 650°C, where a measurable decrease was observed.

Figure 9A and Table 6 also demonstrate that the four reheats above MTT of the CGHAZ caused insignificant hardness reduction compared to a single reheat above MTT. This result demonstrates that most of the hardness reduction is attributed to the first reheat, and multiple reheats do not significantly affect the tempering response of Fe-10Ni weld metal. A similar response to tempering by multiple subcritical reheats above the MTT was found in low-alloy steels (Refs. 13, 36).

Steels with martensitic transformation usually have a larger gap between their MTT and A_{C1} temperatures. Sub-critical reheating of such steels, using short-term high-temperature thermal cycles, has been shown to temper the original martensitic microstructure. Short-term tempering often occurs at peak reheat temperatures above the conventional post-weld heat temperatures. For such steels, empirical relationships were developed to quantify the tempering response to sub-critical reheating above the MTT temperature (Refs. 13, 14). No such equations could be developed for Fe-10Ni steel weld metal due to its short MTT – A_{C1} temperature interval of 60°C and weak tempering response.

The weak tempering response is likely due to the low carbon content in the Fe-10Ni weld metal, which is around 0.018 wt-%. Tempering of fresh martensite involves carbon diffusion out of the strained body-centered-tetragonal (BCT) structure, which relaxes the lattice stress and allows for dislocation motion to commence, resulting in a hardness reduction (Ref. 34). A more detailed description highlighting the five stages of tempering can be found in Ref. 34. The hardness of martensite, as well as the degree of tempering, is linked with the amount of carbon in the material and the tempering temperature (Ref. 34). Therefore, the lower original hardness of the martensite as well as the weaker tempering response in the Fe-10Ni steel weld metal can be attributed to its low carbon content. Although the hardness reduction caused by tempering is not substantial, impact toughness can still be

Table 7 — Hardness of Simulated HAZ Regions of Fe-10Ni Multipass Weld Metal

Weld Region	Peak / Reheat Temperature, °C	Microstructural Category	HV_{10}*	Standard Deviation
As-Solidified Weld Metal	—	As Solidified	292	6.3
CGHAZ	1350	FM-CGHAZ	297	3.14
FGHAZ	1000	FM-FGHAZ	313	9.72
ICHAZ	700	IGHAZ	286	5.35
IC-CGHAZ	1350/700	IC-CGHAZ	282	4.2
Tempered CGHAZ	1350/650	TM-CGHAZ	277	6.18
Tempered FGHAZ	1000/650	TM-FGHAZ	292	6.3

*Average of 5 measurements

influenced by microstructural changes caused by multiple reheating above the MTT. The overall effect of the hardness on impact toughness will be thoroughly detailed in a later publication.

Figure 9B and Table 7 display the measured hardness of the various microstructural regions observed in Fe-10Ni multipass welds. The "tempered" tag in Fig. 9B defines a single reheat above the MTT, resulting in a hardness drop. Apart from the as-solidified category, the HAZ regions were generated in Gleeble™ physical simulations, and hardness was tested. Based on the hardness results described above, several observations can be made regarding the tempering response of Fe-10Ni weld metal. The FGHAZ had a higher hardness than the CGHAZ, which was potentially related to a Hall-Petch effect caused by the difference in grain size between these regions (Refs. 38–41). The lower FGHAZ peak temperature of 1000°C, compared to 1350°C for the CGHAZ, resulted in a smaller effective grain size as previously demonstrated for Fe-10Ni weld metal HAZ (Ref. 10). Subcritical reheats of the CGHAZ and FGHAZ resulted in a similar hardness drop due to tempering.

The IC-CGHAZ, which experienced an intercritical reheat to 700°C, had higher hardness than the CGHAZ tempered with a single reheat to 650°C, Table 7 and Fig. 9B. The IC-CGHAZ underwent a partial transformation to austenite, which transformed to fine-grained fresh martensite on cooling. Only the intercritically reheated martensite that did not transform to austenite experienced partial tempering. Therefore, the intercritical reheat produced a mixed microstructure of tempered and fine-grained fresh martensite, resulting in a higher hardness than in the tempered CGHAZ.

The developed thermal history-microstructure category-hardness relationships are summarized in Table 7 and are related to simulated multiple reheat thermal histories and microstructural categories in Fig. 4 and Table 3, respectively. The latter were developed using the experimentally determined values for A_{C1}, A_{C3}, and MTT. These relationships are expected to accurately capture the tempering behavior of multipass Fe-10Ni weld metal and to enable reliable hardness distribution analyses based on predicted multiple reheat thermal cycle data.

Computational Analysis of Hardness and Microstructure Distribution in Fe-10Ni Multipass Welds

Initial validation of the FEA models of LHI and HHI groove welds

The GMAW-s heat sources, which were developed, calibrated, and validated as previously discussed (Table 4), were used in FEA simulations of the multipass LHI and HHI groove welds using the FEA models defined in Fig. 1. The simulated fusion zone and HAZ surface areas were compared to the experimental LHI and HHI welds, as shown in Fig. 10. The contour markers in Fig. 10 represent the phase transformation temperatures of HY-130 (Ref. 44). The base metal A_{C1} at 732°C, A_{C3} at 854°C, and the melting temperature of 1490°C were used to define the fusion zone and HAZ profile. The melting temperature was determined using the Schiel solidification module in Thermo-calc 2025a (Ref. 31). ImageJ software was used to quantify the fusion zone and HAZ areas visible in the etched macrographs shown in Fig. 10A and 10C. It was assumed that the etched HAZ corresponds to regions heated between the A_{C1} and the solidus temperatures. The predicted surface areas of the fusion zone and HAZ for both FEA models were in good agreement with the measured areas of the experimental welds. Fusion zones surface area agreements further validate the LHI and HHI heat source parameters. The

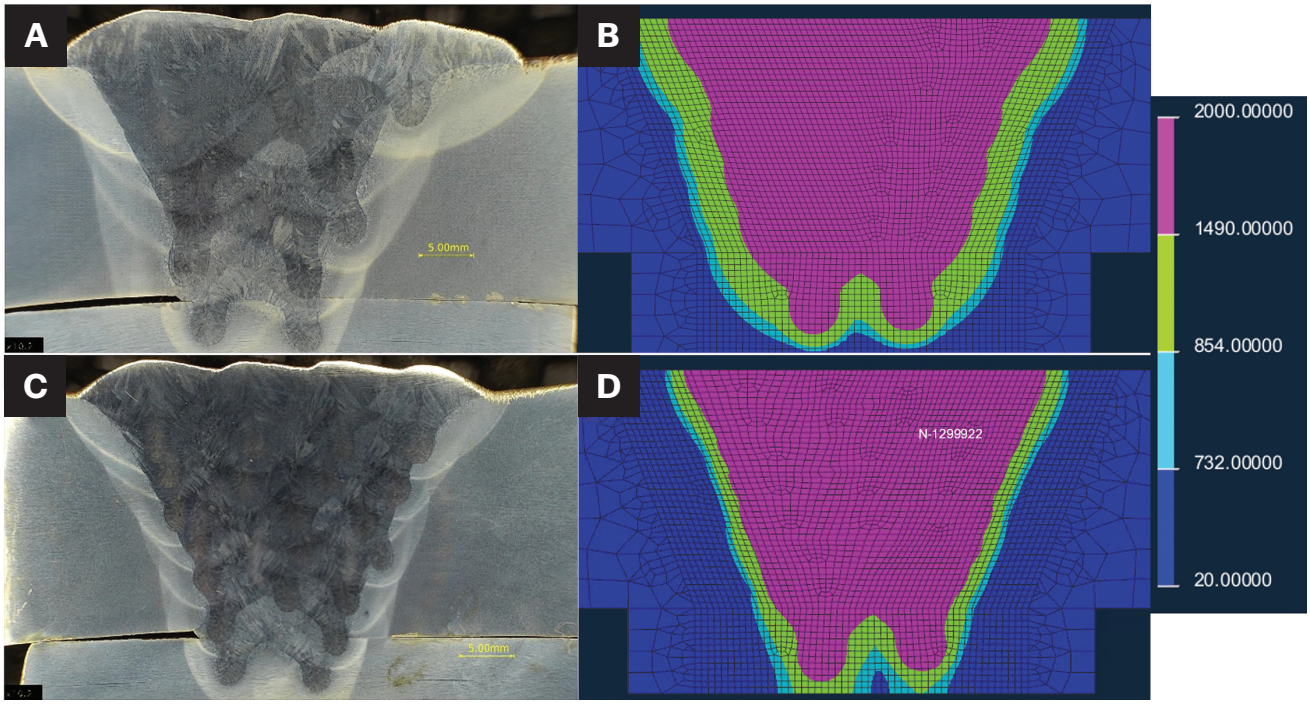


Fig. 10 — Comparison of experimental to simulated fusion zone and HAZ profiles: A and B — HHI process; C and D — LHI process.

Table 8 — Comparison of Measured and Predicted Fusion Zones and HAZ Surface Areas for LHI and HHI Processes

	LHI Surface Area, mm²		HHI Surface Area, mm²	
Location	Measured	Simulated	Measured	Simulated
Fusion Zone	464	452	480	524
HAZ	180	163	271	247

HAZ surface area agreements provide insight that the model was correctly set up and an accurate arc efficiency was used.

Hardness Distribution Analysis in Multipass Fe-10Ni Welds

The FEA model of the MHI buildup, shown in Fig. 2 and defined in the FEA Model Development and Simulation Setup section, was used to simulate the experienced thermal histories throughout the undiluted Fe-10Ni weld buildup. The FEA model used the MHI heat source defined in the Heat Sources Development and Calibration section and Table 4, and the thermal history-hardness relationships described in Development of Thermal History-Microstructure-Hardness Relationship for Fe-10Ni Weld Metal. For each node in the FEA model, the predicted multiple-reheat thermal history was extracted using a post-processing script. The corresponding hardness value was determined using the thermal history-microstructure-hardness relationship defined in Table 7.

Figure 11 compares the computationally generated hardness distribution in the MHI weld buildup with the experimentally measured hardness map. A good correlation is observed, with both maps exhibiting similar trends and hardness distributions. Continuous and repetitive hardness bands are visible around each weld bead. In the as-solidified regions, such as cap passes, relatively low hardness is observed. Moving away from these regions, slight hardening occurs in areas that have been reheated and transformed into a CGHAZ. Additional hardening is observed in the FGHAZ slightly further away. Beyond these hardened zones, there is a consistent band where hardness decreases. The softer bands represent the tempered CGHAZ and FGHAZ as well as the IC-CGHAZ and ICHAZ, which have been shown to have lower hardness than the as-solidified CGHAZ and FGHAZ, Fig. 9B and Table 7. Therefore, the observed softening can be attributed to both intercritical and tempering reheats from subsequent bead depositions. Strong correlation between the computationally generated and measured hardness distributions, in terms of area fraction, is shown in Fig. 11C. The strong correlation between simulated

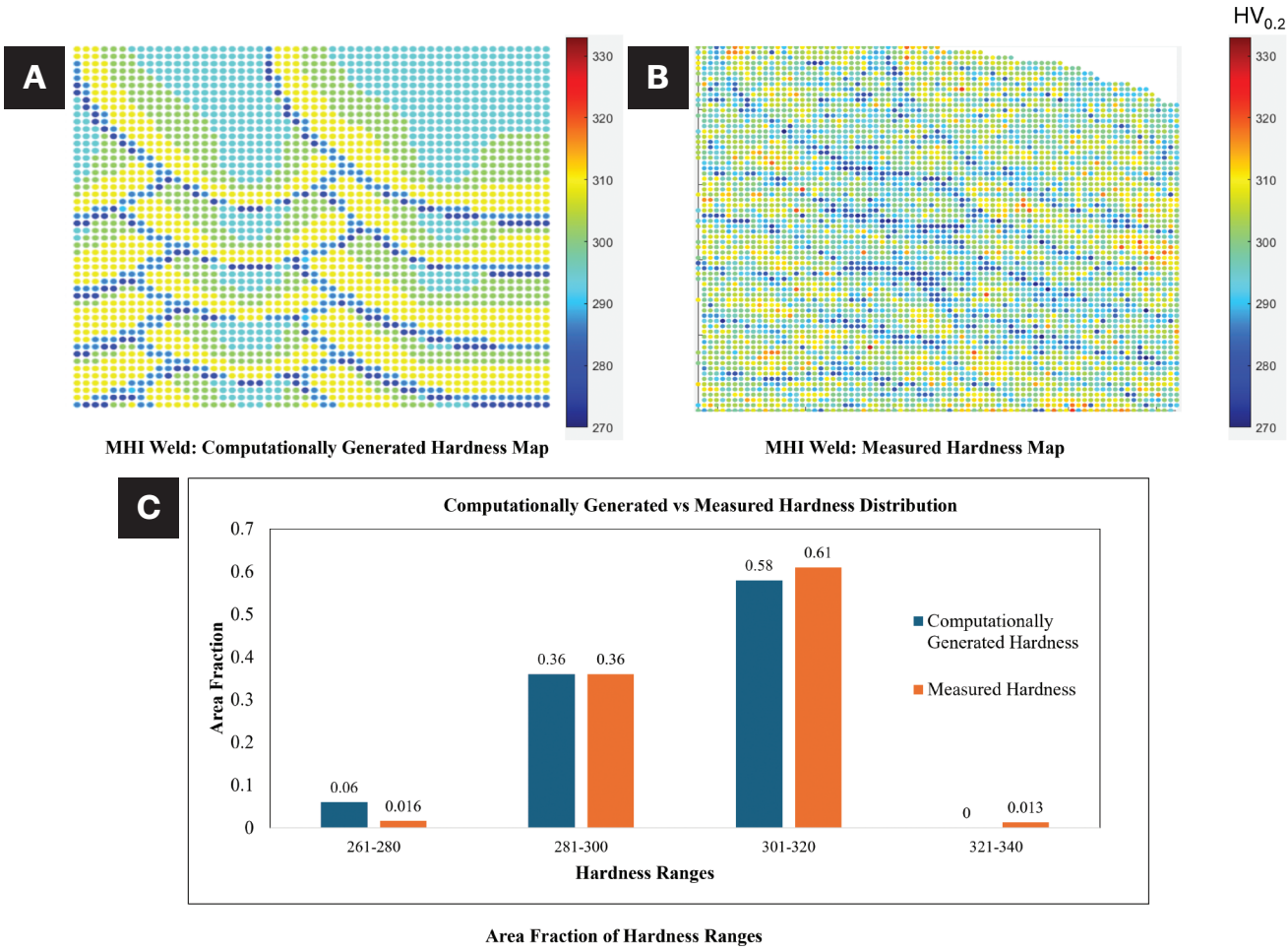


Fig. 11 — Comparison between computationally generated hardness distribution, obtained using the MHI FEA model in conjunction with developed thermal history–hardness relationships, and experimentally measured hardness map of the MHI weld buildup.

and experimental results further validates the accuracy of the thermal cycles predicted by the calibrated FEA model and developed thermal history-hardness relationships. Minor discrepancies between computationally generated and measured values in the contour plots (Figs. 11A and B) and the hardness distribution (Fig. 11C) are due to the FGHAZ spanning a temperature gradient, whereas the computationally generated hardness map uses a single average value for this region. As shown in Fig. 9B and Table 7, the experimental FGHAZ hardness exhibits a standard deviation of ~10, yielding a FGHAZ hardness range of 303-323. This explains why the measured hardness contains some localized values exceeding 320 HV. Figure 11C shows that these values account for 1.2% of the hardness distribution, which is relatively small. Furthermore, the microstructure map indicates a temperature range for the FGHAZ (Fig. 12A). The FGHAZ spans 725°C (A_{C3})–1200°C (Table 3), resulting in hardness scatter due to differences in grain size.

A narrow hardness range, within 40 $HV_{0.2}$ concentrated in 0.97 area fraction of the weld metal, was found in both the computationally generated and experimentally measured hardness maps, Fig. 11. This narrow hardness range is due to the weak tempering response of the Fe-10Ni weld metal, resulting from its low carbon content and the narrow temperature range between MTT and A_{C1}. Although the hardness values are relatively uniform, the slight variation observed may still be relevant when evaluating local impact toughness. Understanding this, as well as the thermal history-hardness relationships developed here, will allow future analysis of hardness distribution with varying heat input for Fe-10Ni weld metal. Reduction of hardness usually indicates regions that have been reheated and tempered, which has been shown to improve impact toughness (Ref. 14). However, it is essential to note that impact toughness is not solely determined by hardness; microstructural features, such as-solidified, coarse-grained weld metal, and reaustenitized HAZ regions, are theorized to play a key role in Fe-10Ni impact behavior (Ref. 10). Therefore, while the comparatively uniform hardness distribution provides a baseline indication of consistency in properties, a more detailed examination of the underlying microstructures is necessary to fully assess the performance of the Fe-10Ni multipass weld metal.

Microstructure Distribution Analysis in Multipass Fe-10Ni Weld Buildup

The FEA model setup for the MHI weld buildup described in the Hardness Distribution Analysis in Multipass Fe-10Ni Welds section was utilized to predict and discretize the microstruc-

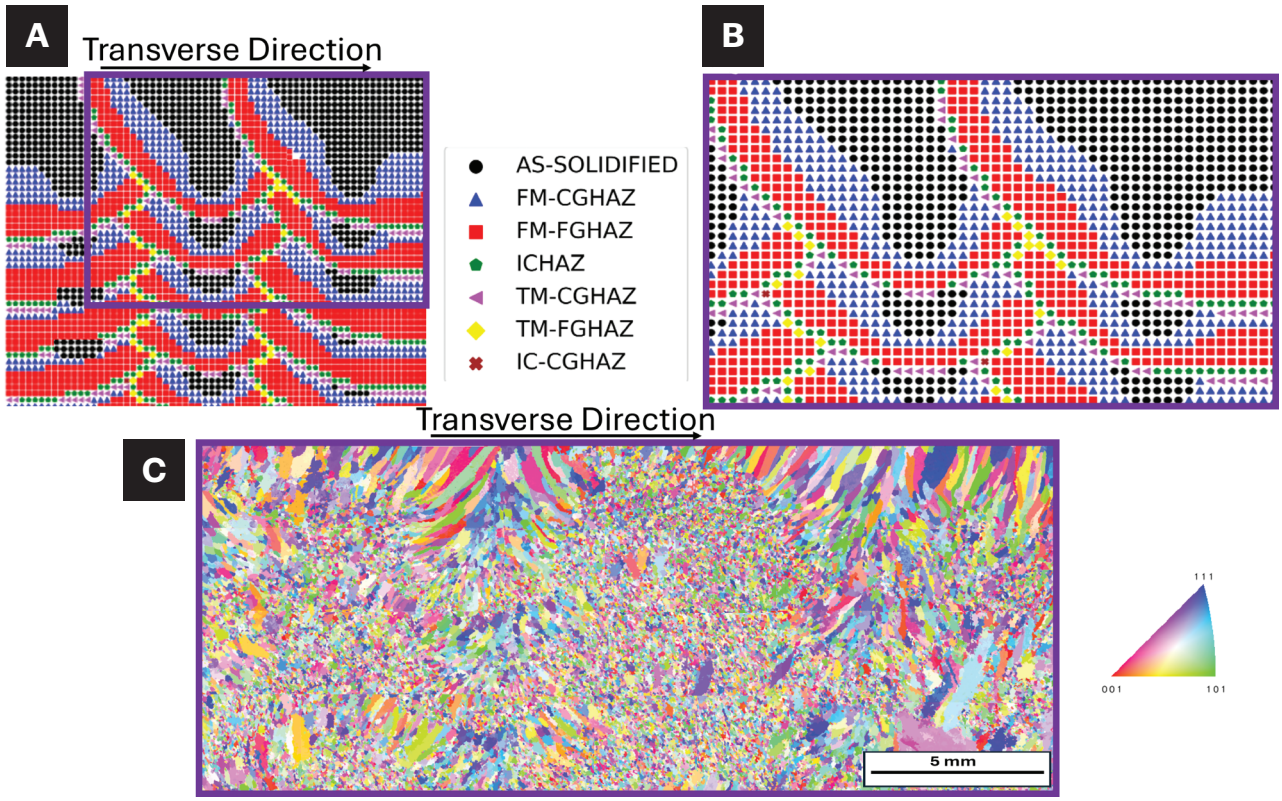


Fig. 12 — A — FEA-generated microstructural map of the MHI multipass weld buildup showing as-solidified regions (black) and reaustenitized regions (colored); B — subsection of A selected for microstructure validation; C — EBSD IPF map of the corresponding subsection from the actual MHI weld buildup.

tural distribution within Fe-10Ni multipass welds. Thermal histories extracted from the FEA model were used to assign a microstructure category to each node within the fusion zone, as defined in Table 3 and Fig. 4. Figure 12A displays the FEA-generated microstructural contour map of the MHI multipass weld buildup.

Similar to the hardness validation described in Hardness Distribution Analysis in Multipass Fe-10Ni Welds, the MHI weld build-up was used for microstructure validation due to the absence of base metal dilution, which can otherwise affect microstructural evolution near the fusion boundary. The validation method involved comparing the computationally generated area fractions of as-solidified and reaustenitized regions with the EBSD quantified ones on the experimental cross-section of the MHI weld buildup. In this study, the term "reaustenitized" was assigned to all microstructural categories that experienced full or partial re-austenitization, as shown in Figs. 4B–G. As-solidified regions are marked in black in the assigned microstructure contour plot, while all other highlighted regions represent reaustenitized microstructures, Fig. 12A. These two classifications were chosen because EBSD analysis can readily distinguish as-solidified grains from reaustenitized ones. To perform the validation, the region from the FEA-generated microstructure distribution map shown in Fig. 12B was compared with an EBSD map of the same size and location on the actual MHI weld buildup in Fig. 12C. Due to the martensitic transformation occurring during cooling, prior austenite grain reconstruction was employed to reveal grain size differences between the as-solidified and reaustenitized regions in the EBSD map. A grain size threshold of 137.7 μm was used to differentiate microstructural regions. Grains exceeding this value were classified as as-solidified, while grains smaller than this value were considered reaustenitized. This threshold was determined from the grain size distribution in the EBSD data (Fig. 13A). Figures 13B and C demonstrate the effectiveness of this threshold: grains below 137.7 μm are smaller and equiaxed, consistent with re-austenitization, whereas grains above this threshold are larger and elongated, indicative of columnar solidification structures. This approach assumes that equiaxed grains are associated with re-austenitization, even though equiaxed grains can form in as-deposited weld metal under certain cooling conditions. Moreover, grain sizes below 137.7 μm constitute the majority of grains, as shown in Fig. 13A, which plots grain diameter versus number of grains. This trend is expected, since most of the buildup experienced reheating and re-austenitization. Figure 14 compares the area fractions of as-solidified and reaustenitized microstructures between the FEA-generated contour plots and the EBSD scan. An excellent correlation is observed, with the as-solidified martensitic microstructure predicted to cover 0.36 of the surface area and experimentally measured to cover 0.38. Accurate quantification of this microstructural constituent is significant in relation to its detrimental effect on impact toughness in Fe-10Ni welds (Ref. 10).

Various similarities can be observed when comparing the computationally generated microstructure contour plot of the MHI weld buildup (Fig. 12B) with the corresponding EBSD

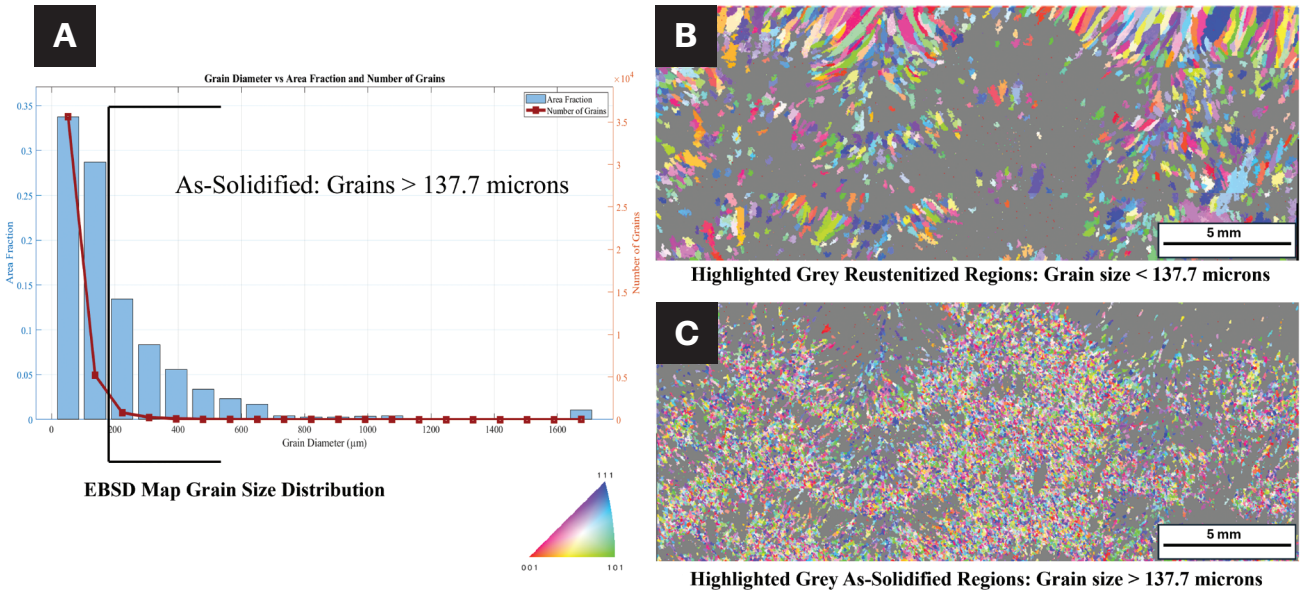


Fig. 13 — A — Grain size distribution obtained from the EBSD map of the MHI weld buildup cross-section in Fig. 12C; B — gray highlighted regions of reaustenitized smaller than 137.7 μm; C — gray highlighted regions of as-solidified grains larger than 137.7 μm.

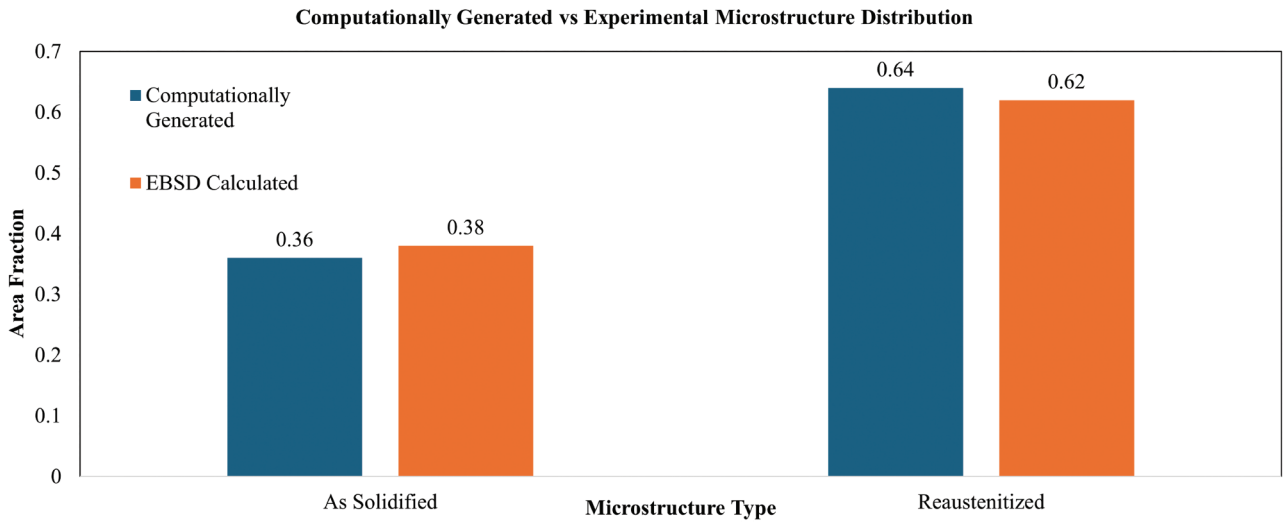


Fig. 14 — Area fractions comparison of FEA-generated and EBSD quantified as-solidified and reaustenitized microstructure in the MHI weld buildup.

map of the same region (Fig. 12C). Both maps show as-solidified regions in the cap passes, characterized in the EBSD map by elongated columnar solidification grain boundaries. The weld bead located to the left of the cap pass is partially reaustenitized in both maps, as indicated by smaller, equiaxed grains in the EBSD scan and colored markers in the predicted contour plot. The remainder of the weld bead consists of the as-solidified microstructure. Moving downward through the weld, both maps display alternating bands of reaustenitized and as-solidified regions. These non-reheated, as-solidified zones persist due to the unique and deep penetration profile associated with Fe-10Ni GMAW-s weld metal, which limits the thermal influence of subsequent passes. The consistency in spatial trends and the close agreement in area fractions between computationally generated and EBSD developed microstructure maps support the effectiveness of the coupled FEA model-property relationship approach in visualizing microstructure distribution in Fe-10Ni multipass welds.

Microstructure Distribution Analysis in Multipass Fe-10Ni Groove Welds

The FEA models set up for the LHI and HHI groove welds described in FEA Model Development and Simulation Setup and Fig. 1 were utilized to predict the microstructural distribution within Fe-10Ni multipass groove welds. Predicted

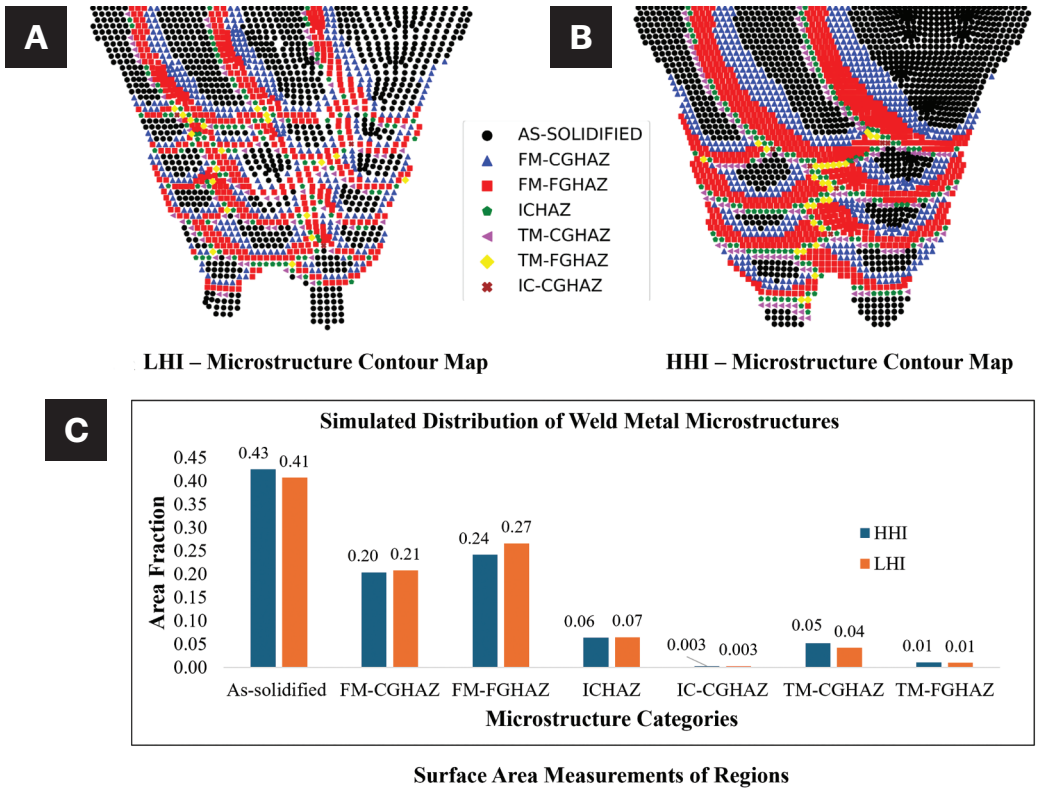


Fig. 15 — FEA-generated microstructural maps in Fe-10Ni multipass groove welds: A — LHI model; B — HHI model; C — surface areas of HAZ regions.

thermal cycles extracted from the FEA model were used to assign one of the microstructural categories listed earlier in Table 3 and Fig. 4 to each node within the fusion zone. The FEA-generated weld metal microstructural contour plots are shown in Figs. 15A and B, and compared by area fraction of microstructural constituents in Fig. 15C. These contour maps demonstrate a significant spatial variation in the distribution of microstructural constituents, predominantly represented by fresh martensite in as-solidified weld metal and weld metal CGHAZ and FGHAZ. The fresh martensite constituent covered 0.87 and 0.89 of the weld metal surface area in the LHI and HHI welds, respectively, including 0.43 and 0.41 area fraction of the as-solidified weld metal.

The microstructural distribution generated for the LHI weld showed a lower area fraction of as-solidified microstructure and a higher area fraction of fresh martensite FGHAZ relative to the HHI weld (Fig. 15C). The as-solidified martensitic microstructure is known to be detrimental to impact toughness, as discussed above. However, the reaustenitized fresh martensite in the FGHAZ may improve impact toughness. Refined grain structures within the FGHAZ have frequently been associated with improved toughness in martensitic steels (Refs. 10, 11, 39, 43, 44). The CGHAZ area fractions were similar for both heat input simulations. The CGHAZ has been shown to have a larger effective grain size than the FGHAZ, which resulted in lower impact toughness associated with that region (Ref. 11). The remaining categories, tempered CGHAZ and FGHAZ, IC-CGHAZ, and ICHAZ, account for a relatively small portion of the weld surface area. This behavior was attributed to the narrow range of 60°C between the MTT and A_{C1} temperatures and the low carbon content of the Fe-10Ni weld metal.

Impact Toughness Considerations

The area fraction of as-solidified versus reaustenitized microstructure is particularly important in the context of the impact toughness of Fe-10Ni GMAW-s welds. Barrick and Dupont (Ref. 10) conducted Charpy V-Notch testing on GMAW-s Fe-10Ni welds and reported that the fracture morphology varied with the microstructure at the notch. Specifically, the as-solidified regions, which have not undergone sufficient reheating or reaustenization, exhibited cleavage fracture, a morphology typically associated with low impact toughness (Refs. 45–47). In contrast, reheated and reaustenization regions displayed ductile dimple fracture morphology. Studies have also characterized alternative welding processes, such as GTAW and GMAW-p, in terms of their influence on microstructure and impact toughness (Refs. 10, 11). GTA welds produced more uniform bead profiles and a greater number of beads and reheats, promoting grain refinement and improved impact toughness. Similarly, GMAW-p welds, which utilized 100% Ar shielding gas, demonstrated enhanced impact toughness due to the absence of deep finger-like penetration patterns and higher oxide content typically observed in GMAW-s using 98% Ar–2% O_2 shielding gas. Based on these findings, potential process modifications include using lower heat inputs to increase the number of reheats or applying temper-bead welding techniques to groove welds to reduce the area fraction of as-solidified weld metal.

The developed numerical simulations framework revealed significant variations in the spatial distribution of microstructure in undiluted Fe-10Ni weld metal deposited with LHI, MHI, and HHI GMAW-s processes, as shown in Figs. 12, 14, and 15. The martensitic microstructures in the as-solidified weld metal and the weld metal CGHAZ were predicted to cover respectively up to 0.42 and 0.21 area fraction of the weld metal surface. Accurate analysis of the content of these microstructural constituents is significant because of their known detrimental effects on the impact toughness in Fe-10Ni welds.

Summary and Conclusions

This study developed and validated an experimental-numerical framework for analyzing the microstructure and hardness distributions in Fe-10Ni multi-pass groove welds produced by GMAW-s processes. The main components of this framework included:

- FEA models in SysWeld™ of the GMAW-s process for groove welds, bead-on-plate welds, and a weld buildup at three heat input levels.
- A heat source model composed of Goldak double ellipsoid and Gaussian truncated conical models, which replicates the deep, narrow "fingerlike" fusion zone profile in GMAW-s welds of Fe-10Ni steel.
- Experimentally derived thermal-history–hardness and thermal-history–microstructure relationships for multipass Fe-10Ni weld metal.

The overall predictive accuracy of the developed framework was confirmed through:

- Heat source model validation by comparison of FEA-predicted thermal cycles to recorded HAZ thermal histories in bead-on-plate LHI, MHI, and HHI welds, and to measured fusion zone and HAZ surface areas in LHI and HHI groove welds.
- Thermal history-hardness relationships and FEA model accuracy validation by comparison of computationally generated to measured hardness spatial distribution in a MHI weld buildup.
- Thermal history-microstructure relationships and FEA model accuracy validation by comparison of computationally generated to EBSD-quantified content and spatial distribution of as-solidified and reaustenitized microstructural constituents in a MHI weld buildup.

It was found that the Fe-10Ni weld metal exhibits a weak tempering response to multiple short-term subcritical reheats imposed by multipass welding. This behavior was attributed to the narrow range of 60°C between the MTT and A_{C1} temperatures and the low carbon content of the Fe-10Ni weld metal. The weak tempering response resulted in a relatively narrow hardness range of about 40 $HV_{0.2}$ in the undiluted Fe-10Ni multipass weld metal.

Undiluted Fe-10Ni weld metal deposited with GMAW-s processes has pronounced variation in the spatial distribution of microstructural constituents. This variation is predominately represented by fresh martensite in the as-solidified weld metal, CGHAZ, and FGHAZ. The fresh martensite microstructures in the as-solidified weld metal and in the CGHAZ were predicted to cover up to 0.43 and 0.21, respectively, in the weld metal of the LHI, MHI, and HHI processes. Accurate FEA-generated distribution of the content of these microstructures is significant because of their known detrimental effect on the impact toughness in Fe-10Ni welds.

The developed numerical simulation framework enables evaluation of the effect of the welding process on the microstructure and properties distribution in multipass welds. Computational process optimization with this framework could help reduce the formation of fresh martensite in as-solidified weld metal and CGHAZ, while increasing the fraction of reaustenitized and tempered regions. The results of this study suggest that the proposed framework can be used to strategically adjust welding process parameters to tailor the microstructure and optimize impact toughness in multipass GMAW welds of Fe-10Ni steel.

Acknowledgments

The authors gratefully acknowledge funding support from the Office of Naval Research. Special thanks to Dr. Daniel Bechetti of the Naval Surface Warfare Center Carderock Division (NSWCCD) for his continued support, guidance, and expert advice. Electron microscopy was performed at the Center for Electron Microscopy and Analysis (CEMAS) at The Ohio State University

References

1. Zhang, X. J. 2012. Microhardness characterisation in developing high strength, high toughness and superior ballistic resistance low carbon Ni steel. *Materials Science and Technology* 28: 818–822. DOI: 10.1179/1743284712Y.0000000015

2. Barrick, E. J. Fundamental studies of phase transformations and mechanical properties in the heat affected zone of 10 wt-% nickel steel. Master's Thesis. Lehigh University, Bethlehem, Pa.

3. Fonda, R. W., and Spanos, G. 2014. Effects of cooling rate on transformations in a Fe-9 pct Ni steel. *Metallurgical and Materials Transactions A* 45: 5982–5989. DOI: 10.1007/s11661-014-2588-3

4. Isheim, D., Hunter, A. H., Zhang, X. J., and Seidman, D. N. 2013. Nanoscale analyses of high-nickel concentration martensitic high-strength steels. *Metallurgical and Materials Transactions A* 44: 3046–3059. DOI: 10.1007/s11661-013-1670-6

5. Kim, J. I., Syn, C. K., and Morris Jr., J. W. 1983. Microstructural sources of toughness in QLT-treated 5.5Ni cryogenic steel. *Metallurgical Transactions A* 14: 93–103. DOI: 10.1007/BF02643742

6. Wu, S. J., Sun, G. J., Ma, Q. S., Shen, Q. Y., and Xu, L. 2013. Influence of QLT treatment on microstructure and mechanical properties of a high nickel steel. *Journal of Materials Processing Technology* 213: 120–128. DOI: 10.1016/j.jmatprotec.2012.08.005

7. Zhao, X. Q., Pan, T., Wang, Q. F., Su, H., Yang, C. F., and Yang, Q. X. 2007. Effect of intercritical quenching on reversed austenite formation and cryogenic toughness in QLT-processed 9% Ni steel. *Journal of Iron and Steel Research International* 14: 240–244. DOI: 10.1016/S1006-706X(08)60086-2.

8. Fe-10Ni steel patent. US10384315.

9. Bechetti, D. H., Sinfield, M. F., and Farren, J. D. Development of a high-strength, high-toughness welding consumable based on the Fe-10Ni steel system.

10. Barrick, E. J., and DuPont, J. N. 2020. Microstructural characterization and toughness evaluation of 10 wt% Ni steel weld metal gas tungsten arc and gas metal arc weld fusion zones. *Materials Science and Engineering A* 796: 140043. DOI: 10.1016/j.msea.2020.140043

11. Barrick, E. J., and DuPont, J. N. 2021. The influence of martensitic microstructure and oxide inclusions on the toughness of simulated reheated 10 wt% Ni steel weld metal multi-pass fusion zones.

Materials Science and Engineering A 801: 140336. DOI: 10.1016/j.msea.2020.140336

12. Jang, E., Luo, Y., Alexandrov, B., McCracken, S. L., Tatman, J., and Barborak, D. 2022. Quantification of the tempering response for temper bead welding of SA-508 low alloy steel. *ASME*. DOI: 10.1115/PVP2022-84884

13. Stewart, J., and Alexandrov, B. 2021. Quantification of the hardness response in the heat-affected zone of low alloy steels subjected to temper bead welding. *Journal of Manufacturing Processes* 66: 325–340. DOI: 10.1016/j.jmapro.2021.04.008

14. Jang, E., Alexandrov, B., McCracken, S., and Barborak, D. 2024. Tempering procedure effects on the impact toughness in simulated heat affected zone of Grade 22 steel. *Journal of Pressure Vessel Technology* 146. DOI: 10.1115/1.4065810

15. Jang, E., Alexandrov, B., McCracken, S. L., and Barborak, D. Comparison of impact toughness properties in Grade 22 steel HAZ after PWHT and temper bead welding. *Journal of Pressure Vessel Technology* 146. DOI: 10.1115/1.4065810

16. Stewart, J. 2019. Temper bead welding for dissimilar metal welds and overlays. PhD diss. The Ohio State University, Columbus, Ohio.

17. Jang, E. 2024. Tempering kinetics and carbide precipitation in low alloy steel heat affected zones in temper bead welding. PhD diss. The Ohio State University, Columbus, Ohio.

18. Shackleton, D. N. 1974. Shielding gas mixtures for high quality mechanized GMA welding of Q&T steel. *Welding Journal*.

19. Kiran, D. V., Cheon, J., Arif, N., Chung, H., and Na, S. -J. 2016. Three-dimensional finite element modeling of pulsed AC gas metal arc welding process. *The International Journal of Advanced Manufacturing Technology* 86: 1453–1474. DOI: 10.1007/s00170-015-8297-2

20. Yang, Z., and Debroy, T. 1999. Modeling macro- and microstructures of gas-metal-arc welded HSLA-100 steel. *Metallurgical and Materials Transactions B* 30: 483–493. DOI: 10.1007/s11663-999-0082-x

21. Essers, W., and Walter, R. 1981. Heat transfer and penetration mechanisms with GMA and plasma-GMA welding. *Welding Journal* 60: 37–42.

22. Kumar, S., and Bhaduri, S. C. 1994. Three-dimensional finite element modeling of gas metal-arc welding. *Metallurgical and Materials Transactions B* 25: 435–441. DOI: 10.1007/BF02663394

23. Goldak, J., Chakravarti, A., and Bibby, M. 1984. A new finite element model for welding heat sources. *Metallurgical Transactions B* 15: 299–305. DOI: 10.1007/BF02667333

24. Azar, A. S., Ås, S. K., and Akselsen, O. M. 2012. Determination of welding heat source parameters from actual bead shape. *Computational Materials Science* 54: 176–182. DOI: 10.1016/j.commatsci.2011.10.025

25. Kik, T. 2020. Heat source models in numerical simulations of laser welding. *Materials* 13: 2653. DOI: 10.3390/ma13112653

26. Farrokhi, F., Endelt, B., and Kristiansen, M. 2019. A numerical model for full and partial penetration hybrid laser welding of thick-section steels. *Optics & Laser Technology* 111: 671–686. DOI: 10.1016/j.optlastec.2018.08.059

27. Rahman Chukkan, J., Vasudevan, M., Muthukumaran, S., Ravi Kumar, R., and Chandrasekhar, N. 2015. Simulation of laser butt welding of AISI 316L stainless steel sheet using various heat sources and experimental validation. *Journal of Materials Processing Technology* 219: 48–59. DOI: 10.1016/j.jmatprotec.2014.12.008

28. ASTM International. Standard practice for quantitative measurement and reporting of hypoeutectoid carbon and low-alloy steel phase transformations. ASTM A1033-18.

29. ASTM International. Standard practice for determining average grain size using EBSD in fully recrystallized polycrystalline materials. ASTM E2627-13.

30. Schwartz, A.J. 2009. Electron Backscatter Diffraction in Materials Science. Springer.

31. Thermo-Calc Software. TCFE14 steels/Fe-alloys database.

32. Champagne, O., and Pham, X. -T. 2020. Numerical simulation of moving heat source in arc welding using the element-free Galerkin method. *International Journal of Heat and Mass Transfer* 154: 119633. DOI: 10.1016/j.ijheatmasstransfer.2020.119633

33. Dornelas, P. H. G., Payão Filho, J. D. C., Farias, F. W. C., Moraes e Oliveira, V. H. P., Moraes, D. D. O., and Zumpano Júnior, P. 2020. FEM-thermodynamic simulation methodology to predict the influence of t8/5 on CGHAZ. *Journal of Manufacturing Processes* 60: 520–529. DOI: 10.1016/j.jmapro.2020.10.082

34. Dupont, J. N., and Marder, A. R. 1995. Thermal efficiency of arc welding processes. *Welding Journal* 74: 406s.

35. Barrick, E. J., Jain, D., DuPont, J. N., and Seidman, D. N. 2017. Effects of heating and cooling rates on phase transformations in 10 wt-% Ni steel. *Metallurgical and Materials Transactions A* 48: 5890–5910. DOI: 10.1007/s11661-017-4379-0

36. Jang, E., Alexandrov, B., McCracken, S. L., and Barborak, D. 2023. Comparison of impact toughness properties in Grade 22 steel HAZ after PWHT and temper bead welding. ASME. DOI: 10.1115/PVP2023-106089

37. Bhadeshia, H. K. D. H., and Honeycombe, S.R. The tempering of martensite.

38. Easterling, K. E. 1983. Introduction to the Physical Metallurgy of Welding. Butterworths.

39. Kaijalainen, A. J., Suikkanen, P. P., Limnell, T. J., Karjalainen, L. P., Kömi, J. I., and Porter, D. A. 2013. Effect of austenite grain structure on strength and toughness of martensite. *Journal of Alloys and Compounds* 577: S642–S648.

40. Simm, T., Sun, L., McAdam, S., Hill, P., Rawson, M., and Perkins, K. 2017. Influence of PAG size on maraging steel properties. *Materials* 10: 730.

41. Abson, D. J., and Jonas, J. J. 1970. The Hall–Petch relation and high-temperature subgrains. *Metal Science Journal* 4: 24–28.

42. Cincotta, P. E. 1981. The effects of simulated welds on HY-130 microstructure. Master's thesis, Naval Postgraduate School, Monterey, Calif.

43. Morito, S., Yoshida, H., Maki, T., and Huang, X. 2006. Effect of block size on strength of lath martensite. *Materials Science and Engineering A* 438–440: 237–240. DOI: 10.1016/j.msea.2005.12.048

44. Wang, C., Wang, M., Shi, J., Hui, W., and Dong, H. 2008. Effect of microstructural refinement on toughness. *Scripta Materialia* 58: 492–495. DOI: 10.1016/j.scriptamat.2007.10.053

45. Davis, C. L., and King, J. E. 1994. Cleavage initiation in reheated CGHAZ. *Metallurgical and Materials Transactions A* 25: 563–573. DOI: 10.1007/BF02651598

46. Lambert-Perlade, A., Sturel, T., Gourgues, A. F., Besson, J., and Pineau, A. 2004. Modeling cleavage fracture in simulated HAZ. *Metallurgical and Materials Transactions A* 35: 1039–1053. DOI: 10.1007/s11661-004-0030-y

47. Norström, L. -Å., and Vingsbo, O. 1979. Influence of nickel on toughness in martensite steels. *Metal Science* 13: 677–684. DOI: 10.1179/030634579790434321

SALMAN MATAN (*matan.6@osu.edu*) and **BOIAN ALEXANDROV** are with Welding Engineering Program, Department of Materials Science and Engineering, The Ohio State University, Columbus, Ohio.